



Contents lists available at [ScienceDirect](#)

Journal of Electron Spectroscopy and Related Phenomena

journal homepage: www.elsevier.com/locate/elspec



State-of-the-art attosecond metrology

M. Schultze^{a,b,*}, A. Wirth^a, I. Grguras^a, M. Uiberacker^a, T. Uphues^a, A.J. Verhoef^a, J. Gagnon^a, M. Hofstetter^b, U. Kleineberg^b, E. Goulielmakis^a, F. Krausz^{a,b}

^a Max-Planck-Institut für Quantenoptik, Hans-Kopfermann-Str. 1, D-85748 Garching, Germany

^b Department für Physik, Ludwig-Maximilians-Universität, Am Coulombwall 1, D-85748 Garching, Germany

ARTICLE INFO

Article history:
Available online xxx

Keywords:
Attosecond spectroscopy
Streaking
Tunnel ionization
High-harmonic-generation
Ultrashort laser
Transient absorption

ABSTRACT

Tracking and controlling electron dynamics in the interior of atoms, molecules as well as in solids is at the forefront of modern ultrafast science [1–5]. Time-resolved studies of these dynamics require attosecond temporal resolution that is provided by an ensemble of techniques consolidated under the term “attosecond metrology” [6,7]. This work reports the development and commissioning of what we refer to as next-generation attosecond beamline technology: the AS-1 attosecond beamline at the Max-Planck Institute of Quantum Optics. It consists of a phase-stabilized few-cycle laser system, for the generation of XUV radiation, and modules tailored for the spectral filtering and isolation of attosecond pulses as well as for their temporal characterization. The setup produces the shortest attosecond pulses demonstrated to date and combines them with advanced spectroscopic instrumentation (electron-, ion- and XUV-spectrometers). These pulses serve as temporally confined trigger events (attosecond streaking and tunneling spectroscopy) or probe pulses (attosecond absorption and photoelectron spectroscopy) enabling attosecond chronoscopy to be applied to a broad range of systems belonging to the microcosm.

© 2011 Published by Elsevier B.V.

1. Introduction

Experiments with attosecond resolution, particularly those utilizing the generation of high harmonic radiation, are necessarily very sensitive to the overall waveform of the driving laser field. The measurement, the precise and reproducible control of the carrier envelope phase, or more generally the waveform of the laser pulses combined with high temporal stability is the key aspect of the laser sources employed in the experiments. With decreasing pulse durations, experimental results become significantly more sensitive to variations of the carrier envelope phase. Besides the reproducibility of the characteristics of the laser pulses, the mechanical stability of the experimental system has to be a main focus of attention to perform attosecond pump–probe experiments in an interferometric setup. Investigations with a temporal resolution of 100 as require mechanical stability better than a few-nanometers over several hours.

2. Generation and measurement of few-cycle laser pulses

To generate the few-cycle NIR pulses required by experiments providing contemporary attosecond resolution we employ a

commercially available chirped-pulse-amplification system (Femtopower Compact Pro, Femtolasers Produktions GmbH) [8,9] that we adapted according to the needs of attosecond experiments. The amplifier system (Fig. 1) is seeded by an ultra broadband Ti:sapphire oscillator, emitting pulses of about 6 fs with an output power of 300 mW at 78 MHz [10]. Before seeding the amplifier (seed pulse energy ~1 nJ) the oscillator pulses are dispersively stretched to 15 ps in bulk material. After the fourth pass of the amplification, a Pockels cell is installed in the beam path, reducing the repetition rate to 3 kHz. A total of 9 passes through a Ti:Sa crystal pumped with ~20 W/3 kHz at 532 nm result in a pulse energy of 1.2 mJ. Subsequent recompression takes place in a hybrid prism/positive dispersive mirror-compressor. The prism compressor is modified to overcompensate the positive chirp the amplified pulses carry; the pulses therefore maintain their negative chirp throughout the final prism and are not subject to self-phase modulation (SPM) which would narrow and modulate the spectrum and thus hinder the final temporal compression of the pulses. The full compression takes place by reflection off positive-dispersion chirped mirrors where SPM does not occur, thereby, sub-25 fs pulses (full-width at half maximum – FWHM) extending over a spectral width of 65 nm and energy of 900 μJ [11] are achieved.

The amplified pulses are focused ($f=1.8$ m) into a 1 m long hollow-core fiber (FiberTech GmbH) with an inner diameter of 250 μm, that is filled with neon at a pressure of ~2 bar. Non-linear propagation of these pulses in the hollow-core waveguide results in (see Fig. 1) the broadening of their spectrum, primar-

* Corresponding author at: Max-Planck-Institut für Quantenoptik, Hans-Kopfermann-Str. 1, D-85748 Garching, Germany.

E-mail address: martin.schultze@mpq.mpg.de (M. Schultze).

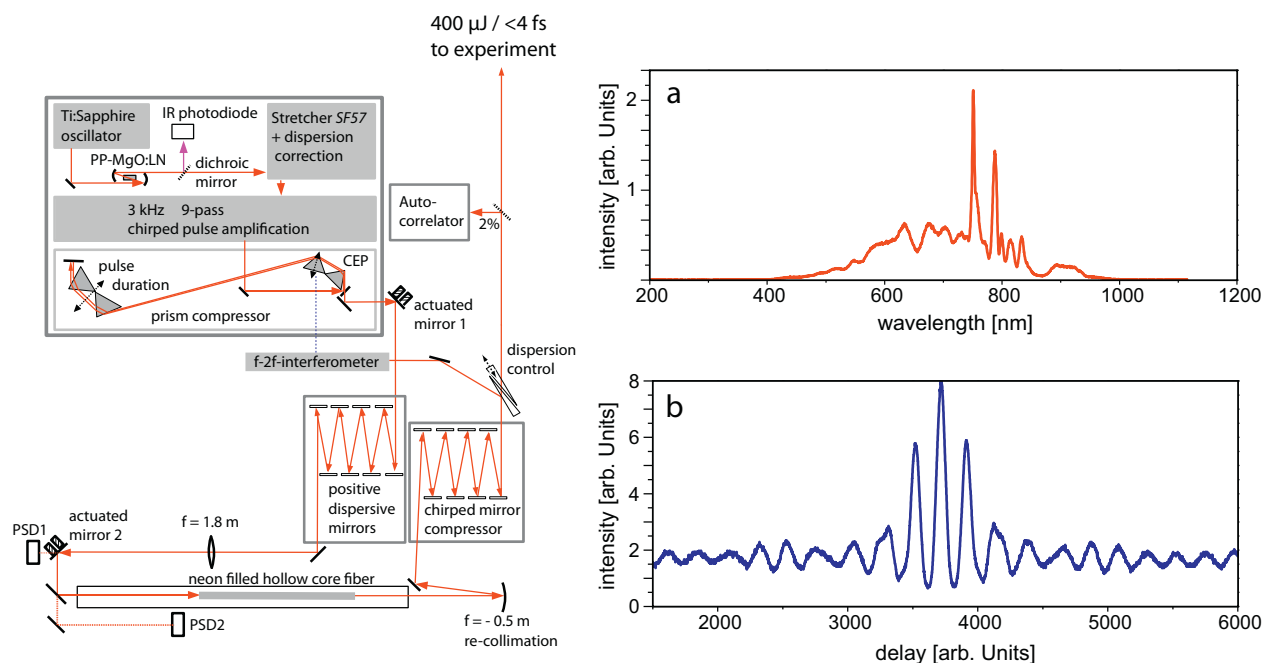


Fig. 1. Schematic laser setup. The left panel shows the Ti:Sa oscillator/9-pass amplifier system with the subsequent pulse-broadening and compression stages including a gas filled hollow core fiber and chirped mirrors for the dispersion management. On the right a typical spectrum achieved after spectral broadening the Ti:Sa output in the fiber is shown (panel a) and the corresponding second order autocorrelation measured after recompression of the pulses in a chirped mirror compressor. The calculated pulse duration is below 4 fs and the pulses carry energy of about 400 μJ at the repetition rate of 3 kHz.

ily due to self-phase-modulation but also because of processes like self-steepening and ionization-induced blue shift [12,13]. The broadened pulses are recompressed to a duration of <4-fs following 8 reflections off low-loss chirped mirrors optimized for the wavelength range of 500–1000 nm [14]. The transmission through the fiber is above 50%. The additional losses the chirped mirrors introduce result in a total transmission of $\sim 45\%$ and pulse energies of 400 μJ after recompression. For the long-term stability for attosecond experiments, a commercial beam stabilization system [15] is used to track the beam pointing with two position sensitive detectors (PSD in Fig. 1), and compensates for beam displacements at the exit of the laser with two piezo-actuated mirrors.

3. Controlling the carrier envelope phase (CEP)

For laser pulses that last only a few oscillations of the light field, the actual evolution of the electric field inside the pulse envelope, rather than just the cycle-averaged intensity, becomes relevant to the experiment. Such ultrashort pulses are usually described in terms of the offset between the maximum of the intensity envelope and the peak of the electric field waveform that oscillates at the central carrier frequency. This temporal offset divided by the period of the carrier wave, is dubbed carrier envelope phase (CEP). For broadband laser pulses, the propagation in a dispersive medium produces a difference in phase and group velocity resulting in a slippage of the carrier wave under the envelope. Two consecutive pulses may suffer a phase shift such that a certain waveform has a recurrence period of $2\pi/\Delta\varphi$, corresponding to a offset frequency f_{offset} of the oscillator's frequency comb [16,17].

In the case of the ultra broadband output of femtosecond oscillators, the so-called f -to-zero technique can be employed to track the CEP [18]. This scheme relies on focusing the broadband pulses of the oscillator into a periodically poled nonlinear medium (here periodically poled lithium niobate – PPLN) to generate the difference frequency of its extreme spectral components. Besides that, the bandwidth of the pulses is slightly increased via self-phase modulation. The optical f -to-zero beat signal carrying the CEP infor-

mation is band-pass filtered by a suitable infrared low pass filter and detected on a photodiode. Locking electronics (Menlo Systems) are used to detect the beat frequency and to generate an error signal proportional to the deviation of f_{offset} from the desired value. The error signal is used in a closed loop as feedback signal to drive an acousto-optic modulator that is installed into the beam path of the pump laser (Verdi Coherent). Modulating the pump laser intensity influences the intra cavity nonlinear phase shift providing a feedback loop for the stabilization of f_{offset} . Fig. 1 shows the location of the crystal (PP-MgO:LN) and the IR sensitive photodiode inside the laser system.

In the presented setup, the intra-cavity dispersion is adjusted such that every fourth pulse has, in principle, the same CE phase and therefore an identical waveform. The stabilization is used to compensate for phase drifts that occur due to instabilities introduced by thermal changes or drifts in the pump laser parameters. Details on the stability performance of these systems can be found in [8]. The amplification process of the pulses to mJ level comes along with additional sources of noise. The amplification in 9 passes through a Ti:Sa crystal includes extensive propagation through air (~ 15 m) and numerous optical components. Earlier schemes used for the stabilization of the CEP phase of the amplified pulses have been based on an f -to- $2f$ interferometer that was seeded by a small fraction of energy (<1%) of the compressed pulses at the exit of the amplifier [19]. The relatively narrow output spectrum of the laser amplifier does not allow for a direct f -to- $2f$ measurement but needs the spectrum to be broadened in a filament by means of white light generation. This filament is usually realized in a sapphire crystal and is very sensitive to fluctuations in the intensity; this dependency translates intensity fluctuations into artificial phase noise in the detection.

Here, we present an upgrade of the scheme for the detection and compensation of the carrier-envelope phase of few-cycle pulses. The detection module is installed at the exit of a chirped mirror compressor after the hollow core fiber. The octave-spanning bandwidth of the spectrum negates the need for additional spectral broadening, and furthermore, the phase noise accumulated inside

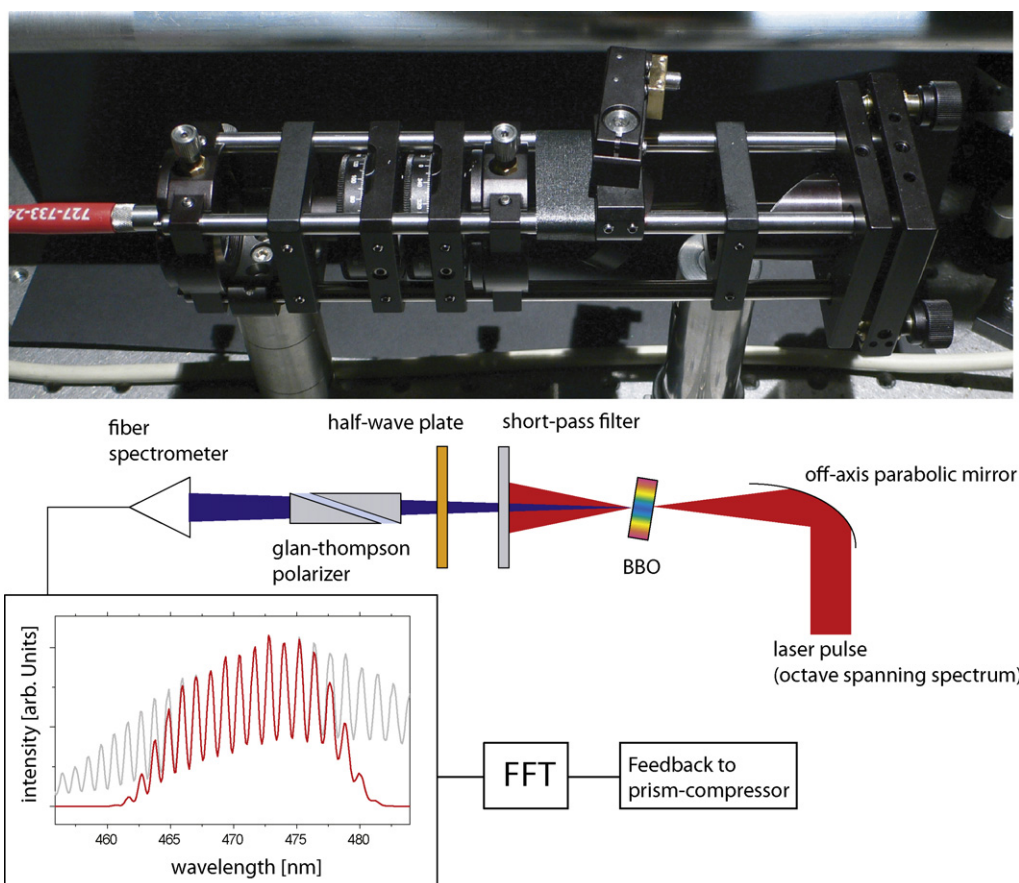


Fig. 2. Compact f -to- $2f$ setup. Around 4% of the amplified and broadened light after the fiber and the chirped mirror compressor are focused by a parabolic mirror into a BBO crystal. The second harmonic light is filtered by a short-pass filter and its polarization is turned to be parallel to the blue part of the fundamental spectrum. A Glan–Thompson polarizer is used to balance the relative intensity and the interference pattern carrying the CE-phase information is observed by a fiber spectrometer. The observed spectral modulation is shown in the inset (grey spectrum). Proper filtering (red spectrum) and subsequent fast-Fourier transformation (FFT) yield a peak at the modulation frequency. The corresponding FFT phase of this frequency peak depends on the carrier-envelope phase. By affecting the insertion depth of one of the prisms of the prism compressor into the beam (Fig. 1) the electronics keep the peak position constant and thus stabilize the CE-phase of the laser pulses. (For interpretation of the references to color in this figure legend, the reader is referred to the web version of this article.)

the hollow-fiber is measured and compensated as well. Experimentally, the carrier envelope phase φ_{CE} is observed as an interference pattern in the spectral region where the fundamental and the frequency doubled light overlap; its implementation is shown in Fig. 2. The period and phase of this interference pattern is retrieved by Fourier analysis of this part of the spectrum and by its evolution. As implied in Fig. 1, the feedback signal is converted into a displacement of one of the prisms inside the prism compressor [20]. Displacing the prism perpendicular to the beam direction almost unchanged, but at the same time it adjusts the amount of material dispersion the pulses accumulate. A standard proportional controller algorithm takes care of adjusting the prism position such that the CE phase changes are counteracted. The achieved phase stability is typically better than 100 mrad RMS which has been confirmed by single shot measurements [21].

4. Temporal and spatial pulse characterisation

For a continuous monitoring of the pulse characteristics, around 4% of the pulse energy is split off behind the chirped mirror compressor and is sent to a second harmonic interferometric autocorrelator. Fig. 1 shows a representative autocorrelation trace that upon evaluation yields a pulse duration of 3.9 fs [22].

Whereas the interferometric second-order autocorrelation comprises a fast diagnostic apparatus and allows fine tuning of the dispersion of the pulses on a daily basis, more elaborate access into the properties of the pulses can be gained via frequency resolved pulse characterization techniques.

To this end, an all-reflective transient grating frequency-resolved optical gating (FROG) device has been incorporated into the setup that is based on the formation of a transient density grating when two time delayed replicas of the pulse impinge on a thin nonlinear medium [23]. The nonlinear medium is a 50 μm thick UV grade fused silica substrate, and introduces limited dispersion to the pulses. The device is therefore extremely broadband and virtually dispersion-free in the spectral range of the laser pulses. Fig. 3 shows a spectrogram recorded with the transient grating apparatus as well as its reconstruction based on commercial software (Femtosec Technologies) [24]. The FROG error for a 512×512 grid was 0.0075, indicating the excellent quality of the reconstruction.

The evaluated pulse length amounts to ~ 4.2 fs, and the retrieval ascertained a positive chirp of 30 fs^2 at 800 nm of the pulses whereas the FL of the spectrum was 3.8 fs. Shorter waveforms that can be composed by these spectra have been sampled via the streaking technique [25]. The information acquired about the spectral phase facilitates the design of particularly adapted chirped mirrors in future upgrades of the beamline.

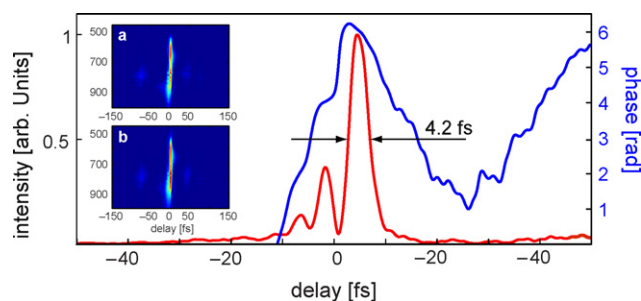


Fig. 3. Time domain picture resulting from a frequency-resolved cross correlation (FROG) measurement of the amplified and compressed laser pulses. The analysis of the trace resulting from the all reflective transient-grating FROG (see text) yields a half-width duration of 4.2 fs. The insets show the measured (a) and the retrieved (b) FROG trace. Across the pulse the spectral phase is adequately flat, indicating the compression of the pulses to a duration close to the Fourier limit (3.7 fs) that is achievable by controlling the dispersion by a pair of thin glass wedges.

In experiments that require high intensities an excellent beam quality is essential. The beam quality of the compressed laser pulses was characterized by means of the M^2 parameter. Using a CCD-camera in combination with a microscope objective, the focal spot size can be accurately determined and the beam diameter as a function of the distance to the focus is obtained using the knife-edge method. The measurement resulted in a very small beam propagation factor of $M^2 = 1.8 \pm 0.1$ with a Bessel-like beam profile caused by the hollow core fiber acting as spatial filter that considerably improves the beam characteristic. These beam parameters come along with a virtually stationary propagation direction since the fiber exit is fixed in space and facilitate a smooth focussing ideal for the generation of high-order harmonics.

5. Pump-probe apparatus

Since a duration of 100 as corresponds to only 30 nm of spatial displacement, special attention has to be turned to the implementation of vibration damping and isolation of the most sensitive units from external mechanical noise sources.

To provide the required stability of the system, the optical breadboards inside the vacuum chambers are mounted on separate pedestals that are directly clamped on the optical table that carries the experiment. These posts are connected to the bottom of the chamber and the walls only by edge welded bellows. The transmission of unavoidable vibrations of the chamber walls, due to the mounted turbo pumps, to optical components located on the breadboards is therefore suppressed. Furthermore, transmission of mechanical vibrations emerging from the roughing pumps to the system is dumped via long hydroformed flexible bellows that are installed into bins filled with silica sand.

6. High-order-harmonic source

The generation of the high harmonic radiation takes place by focusing the few cycle driver pulses onto a thin nickel tube (2 mm inner diameter) filled with neon and kept at a constant backing pressure. The physics of harmonic generation at the atomic and macroscopic levels has been extensively studied [26,27]. The laser drills two holes across the tube, allowing it to enter and exit the tube while ensuring that the hole size is the smallest that transmits the main laser mode. By choosing the tube diameter, the interaction length can be tuned in order to maximize the XUV photon flux. For the sub-4 fs driver pulses with 300 μJ pulse energy, a propagation length of 2–3 mm at a pressure of ~ 250 mbar was identified to maximize the flux of the XUV in the spectral range (70–130 eV).

The efficiency of conversion of the fundamental into XUV photons can theoretically reach the level of 10^{-7} to 10^{-8} [28].

To have a useful amount of photons in the experimental target reabsorption has to be minimized. A significant amount of generated photons is reabsorbed if the partial pressure of the generation gas exceeds 10^{-3} mbar [29]. Two hybrid turbo pumps (Alcatel ATH31+) remove the expanding gas jet close to the interaction volume maintaining a pressure below 10^{-2} mbar in the HHG chamber during operation. For the laser parameters presented here, focus intensities around $1\text{--}8 \times 10^{14}$ W/cm² at a focus diameter of ~ 150 μm (achieved by focusing with spherical mirrors of focal length between 50 and 70 cm) yield the maximum photon flux in an isolated pulse in the energy range between 70 and 130 eV. For high harmonic emission in this energy range neon exhibits the optimum combination between ionization potential and absorption cross section [28]. The XUV generation can be described with a three-step process: electron liberation through tunnel ionization, acceleration of the electron in the laser electric field and subsequent recombination of electron and ion. This three-step model [26,30] relies on tunnel ionization as a first step and therefore predominantly occurs in the most intense on-axis part of the laser focus [31]. Due to the short wavelength of the generated light, together with its high degree of coherence, the XUV radiation is emitted with a small divergence angle as compared to the driving laser pulse. This allows for the spatial separation of the two beams.

After 10 cm propagation in the vacuum chamber that hosts the generation target, the XUV beam and the co-propagating residual IR pulses enter the first differential pumping stage. The reabsorption up to this point is estimated to be below 2% and negligible at any other location of the experimental setup since the pressure of the residual gas drops to less than 10^{-3} mbar.

Between the two differential pumping stages (see figure) an ionization based detector for the XUV (“HH-Meter”) is implemented. Its design is inspired by the ionization chambers that are broadly used in synchrotron facilities [32]. A conductive wire along the tube with a small applied voltage collects the charged fragments that are liberated by ionization of the residual gas and an amplifier suitable for nA currents provide the desired measure of the XUV flux. The signal of the HH-Meter is proportional to the number of electrons and ions created by absorption of XUV photons across the entire emitted spectrum down to energies equal or higher to the ionization potential of neon. Therefore the stability of this signal is only partially related to that of the intensity of the attosecond pulse which is extracted from the cut-off of the emerging spectra. However, as an independent measure of the source stability and flux it is a useful tool that allows one to monitor the XUV signal and identify ideal and stable conditions for performing sensitive experiments. Typically the XUV flux stability recorded with the HH detector is better than 2.5% (standard deviation/mean value).

In the second differential pumping stage, the pressure is further reduced to $\sim 5 \times 10^{-7}$ mbar and a motorized aperture allows for controlling the intensity of the few-cycle pulse that enters the experimental chamber between 0 and ~ 50 μJ .

7. Experimental chamber

At the entrance of the experimental chamber (see Fig. 4), the two collinear beams pass a variable filter setup that permits separation of the beams into the central XUV part and the annular IR part. A laser grade pellicle (15 μm thickness) is prepared to carry in its center a $\varnothing 3.5$ mm free-standing metallic foil to block the remaining NIR light on the beam axis. At the same time, this foil acts as a high-pass filter for the high-harmonic radiation and is chosen to have transmittance characteristics matching the spectral bandwidth required for the experiments. The XUV transmission of thin

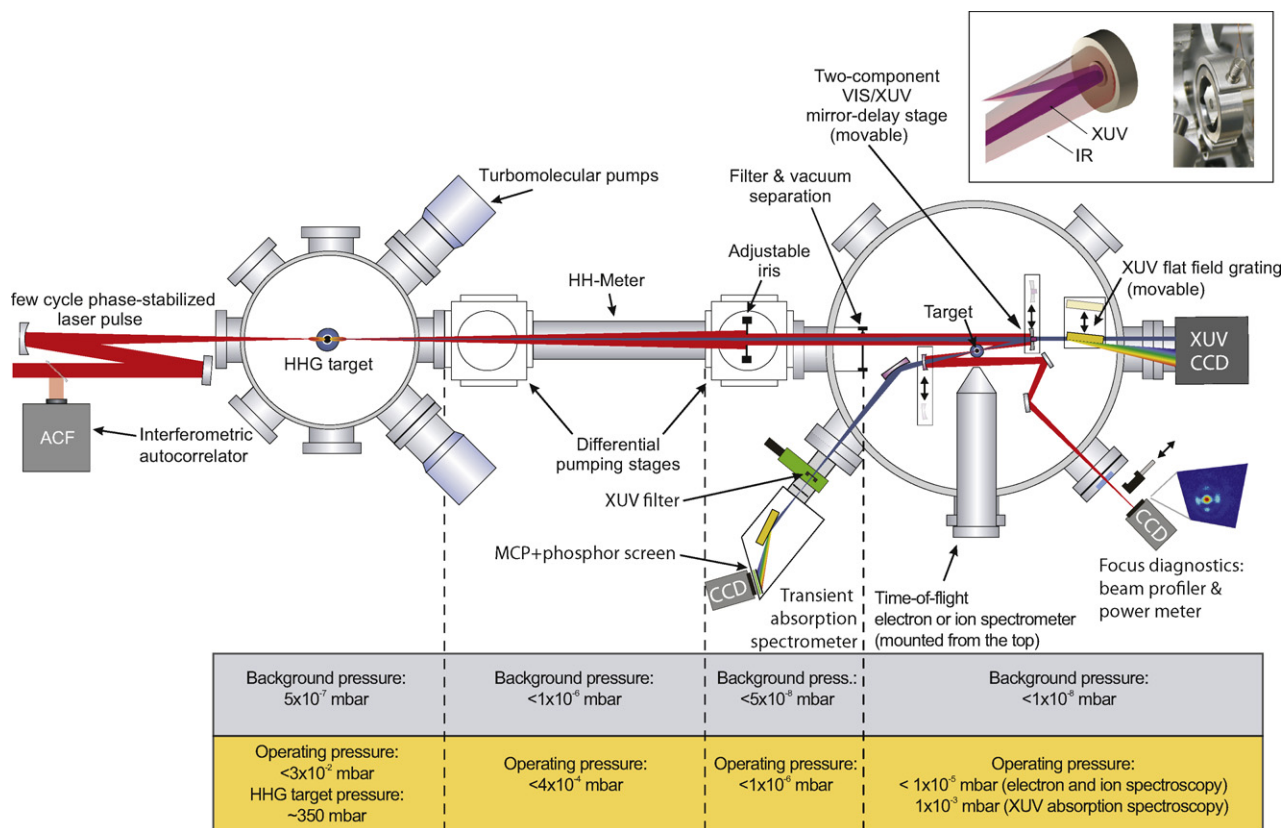


Fig. 4. Experimental setup: few-cycle phase-stabilized NIR laser pulses are focused into a noble gas target (Ne) to produce high order harmonic spectra from which attosecond XUV pulses can be isolated. The remaining NIR pulse and the XUV light propagate through differential pumping stages to prevent the gas used in the generation process from entering the experimental chamber. The “HH-Meter” tracks the ionization of the background gas and therefore provides a direct measure of the XUV flux. The NIR intensity is adjusted by an aperture. A thin metal foil mounted at the center of a laser grade pellicle acts as high pass filter to extract the continuum part of the generated XUV spectrum. The fundamental is transmitted through the pellicle in form of an annular beam around this filter. The two concentric beams are then focused by a double mirror assembly (inset) consisting of a XUV multilayer mirror in the inner part and a silver-coated perforated mirror of the same focal length. XUV and NIR pulses are spatially and temporally overlapped in the Fourier plane while their delay can be adjusted over a range of ± 150 fs by translating the inner mirror along the beam axis using a closed loop piezo stage. Pump-probe experiment can be performed on a variety of gaseous samples and besides the time-of-flight spectra of the emitted photoelectrons (streaking measurements), mass spectra (ionization studies) and the transmitted photon spectrum can be recorded (transient absorption spectroscopy).

metal foils typically used in attosecond experiments is given in Fig. 5 [33]. After that filtering, the two beams impinge on a two-component delay mirror assembly shown in the inset of Fig. 4. The inner mirror is coated by a multilayer structure designed for

high reflectivity in the XUV range. The outer part of the mirror assembly is coated with silver to reflect the laser pulses virtually dispersion-free. Both concave mirrors have a radius of curvature (ROC) of -250 mm. The inner mirror [34] is mounted on a closed

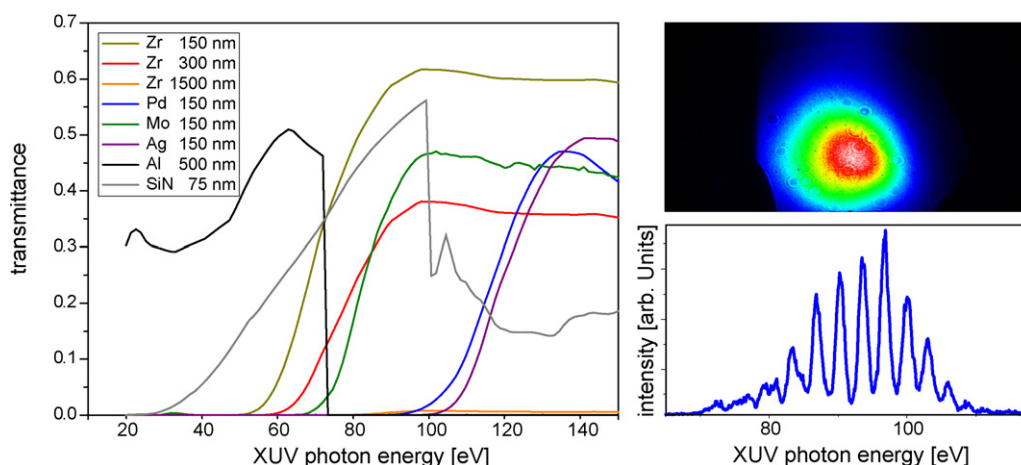


Fig. 5. Filter transmittance vs. photon energy (left panel) [33]. The black and the grey curve depict transmittance edges of aluminum and silicon-nitride that are suited for a calibration of both the electron- as well as the photon spectrometer. The colored curves show the transmission properties for different metals (material and thickness specified in the legend of the graph) that are used in the experiment for wavelength selection of the radiation. High-harmonic beam profile (right panel) and spectrum. The upper image shows the beam profile of the HHG beam on the XUV sensitive camera. The lower panel shows the HHG spectrum as observed in the experimental chamber after transmission of the incident XUV light through a $1.5 \mu\text{m}$ zirconium foil. To demonstrate the spectrometer resolution, the laser bandwidth was restricted to achieve multicycle pulses that generate modulated high-harmonic spectra with the highest possible fringe contrast.

loop controlled piezo stage that allows translation of the mirror along the propagation axis with a resolution better than 2 nm setting the ultimate limit for the smallest possible delay step to the equivalent of 14 as. The double mirror assembly is motorized to move perpendicularly along the incoming beam, and features two independently adjustable angles to precisely position the focus of the two beams in the acceptance volume of the detection device.

For the experiments, it is crucial to perfectly overlap the two pulses reflected off the inner and the outer mirror not only along the beam, i.e. in time but also to accurately superpose them in space. To this end, an imaging system is installed that is based on a concave lens ($f = 15$ cm, $M \sim 20$) and a CCD camera that is placed outside the experimental chamber. Due to its shorter wavelength, the focus of the XUV pulse is safely smaller than the laser focus (~ 25 μ m FWHM).

The double mirror stack focuses the two beams under a narrow angle ($<5^\circ$) such that the focus is located a bit to the side of the incoming beams, the astigmatism and the waveform distortion that result from this aberration are small enough not to bias the experiments. The focal region is located within the acceptance volume of an electron time-of-flight and/or a reflectron mass spectrometer detecting ionic charge states. Given the low absorption cross sections in this energy range and the limited number of photons, the gas pressure in the focal volume should be as high as possible without deteriorating the vacuum conditions over an extended region. To this end, a carbon-coated and grounded glass nozzle (to minimize charging effects) with an inner diameter of ~ 30 μ m effuses a gas as a cone perpendicular to the laser beams. This approach limits the interaction of the attosecond and laser pulses to within a fraction of the focal volume and minimizes averaging effects that could emerge due to a longitudinal phase delay (Gouy phase shift) or non-uniform intensity distributions. Another class of experiments relies on the XUV spectrum transmitted through an ensemble of atoms. For these attosecond transient absorption experiments, a quasi-static gas cell which is similar to the high-harmonic generation target discussed earlier can be installed into the focus. All the in-vacuum motorization is done using vacuum suited translation stages [35].

8. Spatial and spectral characterization of the XUV source

To optimize the XUV source, the direct observation of the direction and spectral distribution of the beam is essential. For these purposes, an imaging spectrometer based on a grazing-incidence flat field grating [36,37] and a back-illuminated CCD camera are located at the exit of the experimental chamber. After the double-mirror assembly is moved out of the beam path, the XUV light can be monitored (Fig. 4). The XUV camera observes either the direct beam, or, after inserting the grating, the spectral extent of the generated XUV light (Fig. 5). The imaging spectrometer has an overall efficiency (grating $\sim 85\%$, CCD-chip $\sim 40\%$) of 34%. Its minimal acquisition time to achieve a statistically significant spectrum is limited by the shortest exposure time of the camera, which is ~ 50 ms. The spectrometer therefore constitutes one of the fastest CE-phase monitoring devices by requiring the accumulation of approximately 150 pulses to provide information about changes in the CE-phase. The spectrometer's resolution is estimated to be around 0.5 eV, therefore the typical spacing of twice the fundamental photon energy (3.2 eV for 750 nm photons) in the harmonic spectra can be clearly resolved as shown in Fig. 5. In order to avoid saturating the CCD chip, the laser light is rejected and the XUV light attenuated by a 1.5 μ m zirconium foil at the entrance of the spectrometer.

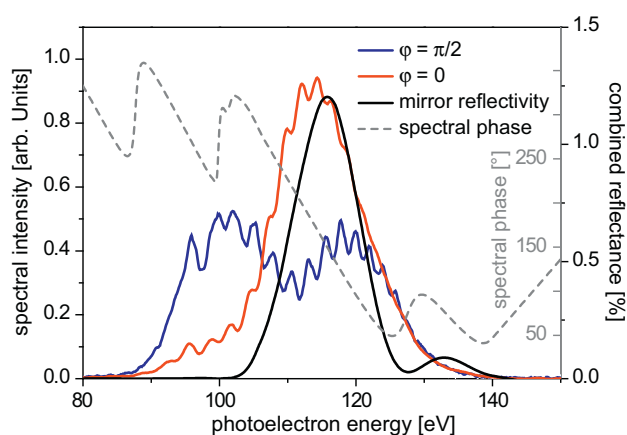


Fig. 6. XUV spectra emanating from the interaction of few-cycle phase stabilized laser pulses with Ne atoms after being transmitted through 1.5 μ m of a free standing Zr foil. The spectra are integrated over ~ 300 shots of the laser. Red/blue curve: spectra of the XUV pulses emitted by few-cycle driver pulses with a CE phase different by $\pi/2$. The high degree of modulation in the spectrum associated to the waveform labeled as $\pi/2$ constitutes the spectral manifestation of a substantial fraction of intensity contained in a satellite pulse in the time domain. To isolate attosecond pulses from the generated spectrum, multilayer mirrors with band-pass characteristics are used. The combined reflectance/transmittance characteristics of a multilayer mirror and the palladium foil are indicated by the black line. The grey dashed curve shows the calculated spectral phase response of the multilayer mirror. (For interpretation of the references to color in this figure legend, the reader is referred to the web version of this article.)

9. Spectral filtering of the XUV light

To make use of the extreme temporal resolution that attosecond pulses offer, an experiment needs to be capable of spectrally selecting and focusing the generated radiation. Given the low conversion efficiency, the focusing should not drastically compromise the energy contained in the attosecond pulse and the temporal characteristics should be preserved. Furthermore, for isolating single attosecond pulses it is furthermore necessary that the XUV optics filter out the modulated part of the spectrum that give rise to a train of attosecond pulses [38].

Elaborate XUV multilayer optics can meet these ambitious demands. These mirrors consist of a series of layers of alternating materials (in the energy range discussed here e.g. molybdenum/silicon or molybdenum/lanthanum) coated on a finely polished concave substrate. By adjusting the relative layer thicknesses, the sequence of materials and the number of layers, the central energy, the spectral response as well as the reflectance of the mirrors can be adjusted to meet the requirements of attosecond experiments. In addition, a proper adjustment of the mirror's spectral dispersion properties of the mirror allows to achieve pulses with durations close to the Fourier limit of the reflected spectra or to set arbitrary spectral phase values ("chirp") according to the needs of a certain experiment [39]. The combined transmittance/reflectance characteristics of the metallic filter and the mirror facilitate the selection of a spectral band in which, with carefully chosen parameters of the generating laser field, the emission corresponds to only one single half cycle of the laser pulse and thus forms an isolated pulse.

The sensitivity of this method is displayed in Fig. 6 showing XUV spectra recorded for different settings of the CE phase of the driver laser pulses matched to the reflectance band of a multilayer mirror supporting 160 as pulses. Recent advances in the laser source development towards pulse durations containing less than two cycles of the laser field [11] allow for the generation of ever broader unmodulated XUV spectra. The combination of state-of-the-art short-pulse lasers with ultra-broadband multilayer mirrors

led to the realization of the first sources that routinely generate XUV pulses of less than 100 as duration [25].

10. XUV pulse intensity

Core-hole excitations, followed by dynamics evolving on an attosecond timescale generally possess low absorption cross sections in the XUV. For example, in the case of direct photoionization of helium 1s electrons at a 90 eV photon energy, the partial cross section amounts to only 5×10^{-1} Mb, while for the first shake-up satellite ($n=2$) it is only 4×10^{-2} Mb [40].

Experimentally, these low cross sections translate into low count rates in the cross correlation experiments described later in the manuscript. Modifications in the generation scheme of the high harmonic light therefore have to be reviewed in consideration of the generated flux within the useful energy band. The number of photons that form the attosecond pulse, however, is not directly measurable and hence is often obtained through rough estimations. The XUV-sensitive camera used to observe photon spectra shown in Fig. 4 can record images of the direct XUV beam. After proper background subtraction and considering the known quantum efficiency of the camera and the integration time, an absolute number of photons after the filters in front of the camera can be extracted. The spectral shape of the attosecond pulse is accessible using the electron spectrometer, since neither the ionization cross section of neon nor the detection efficiency for the electrons vary substantially throughout the bandwidth of interest.

Attosecond streaking together with a FROG analysis of the spectrogram (an example is shown in Fig. 7) can certify the absence of satellite pulses implying that all the energy is contained within a single attosecond pulse [25,41]. The knowledge of the filter transmittance (Fig. 5) and the mirror reflectance (Fig. 6), which can be independently measured at synchrotron sources, allow for the identification of the integral of the photon spectrum after the mirror. The number of photons generated fades dramatically towards higher energies. Due to the fast intensity drop of the harmonic radiation in the cut-off part of the spectrum, only a vigorous suppression of the low-energetic photons allows for the generation of attosecond pulses truly isolated in time. Choosing the right filter material corresponding to a given mirror reflectivity is therefore a crucial point in the reproducible generation of isolated attosecond pulses. The typical XUV flux attainable in isolated pulses amounts to $\sim 5 \times 10^8$ photons per second. A single pulse therefore contains 10^5 photons corresponding to pulse energies of a few pJ [41].

Attosecond time-resolved experiments can be carried out based on three different detection schemes that can be incorporated in the presented apparatus. An electron time-of-flight spectrometer was used for the timing studies of photoionization, while for time resolved experiments on tunnel ionization, the ions were detected by a reflectron type time-of-flight ion spectrometer. Quantum level population dynamics of valence shell electrons are tracked by means of NIR pump–XUV probe absorption spectroscopy.

11. Attosecond streaking metrology and spectroscopy

In the case of electron time of flight spectrometry, the kinetic energy of the electrons under scrutiny is determined by measuring their arrival time on a detector placed in a known distance from the interaction volume. Since the range of kinetic energies of interest is set by the photon energy, causing the excitation to be lowered by the ionization potential of the atom, the most energetic photons detected have a kinetic energy of about 100 eV. The resolution of $\sim 1\%$ of the electron kinetic energy is satisfactory for the experiments carried out, even though it sets a limit to the observ-

able structures in the recorded spectra, which might give additional insight to the processes involved.

In the TOF spectrometer [42], the electrons pass a magnetic shielded drift tube, after which they undergo acceleration. This post acceleration ensures a uniform response of the microchannel plates (MCP), irrespective of the electrons kinetic energy. At the entrance of the flight tube, an electrostatic lens increases the acceptance angle of electrons within a certain range of kinetic energies. The signal measured at the MCP is digitized using a multiscaler card [43] with a minimal time discrimination of 250 ps. The red line in panel c of Fig. 7 shows a typical electron time-of-flight spectrum recorded when neon is ionized with radiation reflected by the multilayer mirror described in Fig. 6. The electron TOF scheme typically yields one count per laser pulse within the experimental bandwidth, using neon as a target gas. This rate is almost independent of the bandwidth response of the multilayer mirror because the mirror's reflectance is inversely related to its bandwidth. The spectrogram shown in Fig. 7 comprises 100 individual spectra and is taken within 30 min, at a delay step size of 100 as. The two spectral contributions can be identified as electrons released from the 2p and 2s subshells of the neutral neon atom. If the attosecond XUV pulse releases electrons in the presence of the laser electric field, the final kinetic energy of the electron is modified.

The net momentum change imparted to the electrons by the laser field depends on the time delay between the two pulses. A set of electron TOF spectra are recorded over a range of delays between them. The resulting spectrogram is shown in Fig. 7 and it is immediately evident that this so called “streaking spectroscopy” [2,6,7,44] samples the temporal evolution of the laser electric field (more precisely its associated vector potential). A more involved analysis along the lines of frequency-resolved optical gating (FROG) [45–47] additionally allows for reconstructing the temporal structure of the attosecond pulse, including its temporal and spectral phase. Streaking experiments enable the temporal characterization of the attosecond burst in the high harmonic process when performed on electrons liberated from only one specific atomic state [48,49]. The growing ability to shape the XUV emission according to the needs of the experiment extends the technique to a wider spectral range and thus to the study of multiple photoemission lines. For a spectrogram as shown in Fig. 7, it is found that the emission of electrons from the 2s shell of neon precedes the liberation of those from the 2p shell [50] by about 20 as. These results highlight the unprecedented temporal resolution offered by attosecond streaking spectroscopy, and how (in combination with the powerful FROG technique) it gives access to subtle timing features in the photoemission occurring in gases and solids [3] that hitherto remained experimentally inaccessible.

12. Attosecond ionization spectroscopy

In combination with a mass spectrometer, the presented pump–probe system constitutes a sampling system capable of tracing the relaxation dynamics of core excited ions with attosecond resolution [51,52]. The ion population transfer following the attosecond XUV excitation is tracked with a reflectron type TOF ion spectrometer [53]. Its working principle is based on time-of-flight mass spectrometry where ions are accelerated in an electric field to the same kinetic energy with the velocity of the ion depending on the mass-to-charge ratio. After the ionization event, the ratio between different charge states can be determined as shown in Fig. 8. We have chosen a reflectron spectrometer because the ion mirror setup grants two important facilities. On the one hand it is possible to set its dispersion characteristics for the drifting ions, to compensate for an energy spread of the generated ion packet due to e.g. delayed ion formation and space charge effects and thus

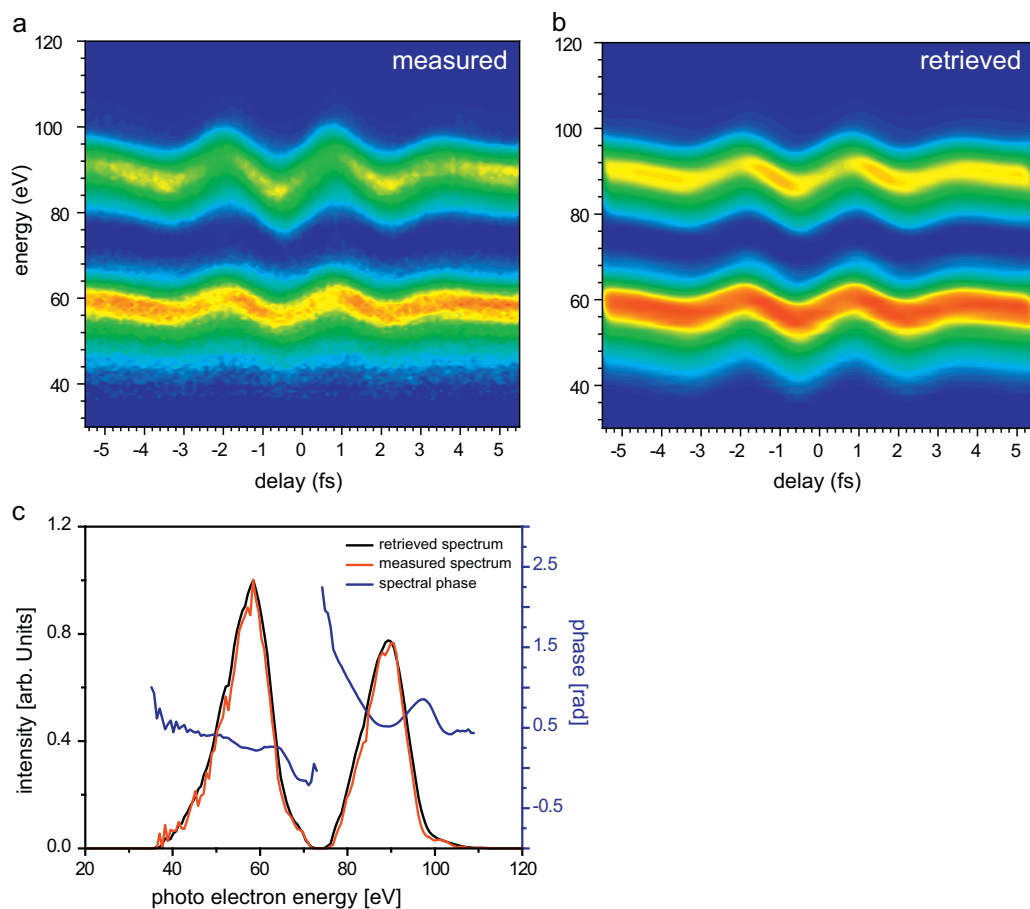


Fig. 7. Measured (a) streaking spectrogram for the ionization of neon from the 2p and the 2s shell after absorption of a 200 as XUV pulse. The streaking spectrogram is processed with a frequency-resolved optical gating (FROG) code to identify the temporal structure of the XUV pulse. The similarity of the measured (red) and the retrieved (black line) photoelectron spectrum shown in panel c highlights the accuracy of the FROG analysis that additionally yields the spectral phase (blue line) of the electron wave packet released after XUV absorption. This spectral phase comprises information about the relative timing of the two emissions and the phase of the emission itself. (For interpretation of the references to color in this figure legend, the reader is referred to the web version of this article.)

improve the attainable resolution. On the other hand, the ion mirror can act as an energy filter that permits the detection of ions exclusively created in a confined volume inside the laser focus providing access to truly intensity resolved ionization yields [54].

The photon energy of the XUV pulses used for that experiment was centered at 93 eV and exhibited a bandwidth of 9 eV, corresponding to pulses of ~ 250 as in duration. The data are accumulated using an amplifier in combination with a multiscaler card. The overall resolution of the spectrometer and the detection electronics allows a $\Delta m/m$ ratio of better than 10^{-3} .

An illustrative application of attosecond ionization spectroscopy is to explore the inner-shell relaxation times of xenon atoms as presented in Fig. 8. For the 91 eV XUV photons applied in this experiment, the cross-section for single ionization of xenon is much smaller than for double and even triple ionization accompanied by secondary processes such as Auger decay or autoionization. The resulting temporal evolution of the number of atoms in the Xe^{4+} state reveals the characteristic time structure of two subsequent Auger decays [51]. In this experiment, one attosecond pulse released about 5 ions distributed over the different charge states.

13. Attosecond transient absorption spectroscopy

As depicted in Fig. 4, a second XUV spectrometer enables the observation of the spectral content of attosecond pulses after their propagation through an ensemble of atoms within a confined inter-

action volume. By retracting a movable mirror which was directing the beam into the imaging system and onto the CCD, both beams impinge on a concave (ROC = -340 mm) multilayer broadband XUV optic whose reflectivity was optimized for an angle of incidence of 67° . This concave optic creates a line focus in the plane of the entrance slit of the spectrometer. A suitable thin metal filter (here zirconium of 150 nm thickness) in front of the entrance slit blocks the fundamental NIR radiation. Spectral dispersion of the XUV light takes place in a commercially available Rowland-circle based spectrometer (MCPerson, Model 248/310, no exit slit), utilizing a concave grating with 2400 grooves per millimeter. Its detection is realized by means of a microchannel plate in combination with a phosphor screen and fiber-coupled CCD camera. This detection scheme inherits a heavily reduced sensitivity to the fundamental NIR light than compared to XUV sensitive CCD cameras, which is a prerequisite for obtaining a high signal-to-noise ratio of the XUV spectra. In this class of experiments, the NIR pulse serves as the pump and the attosecond XUV pulse acts as the probe pulse which can read out characteristic information of the target atoms, which in turn translates to resonant and non-resonant absorption features in its spectrum, as shown in Fig. 9 (upper panel). Here, a sub-4 fs NIR pulse strong-field ionizes at 5.5×10^{14} W/cm² neutral krypton (Kr) atoms in the experimental interaction volume comprising a gas pressure of ~ 80 mbar. The remaining neutral atoms and strong-field-created ions are then probed via a delayed ~ 150 as XUV pulse centered at ~ 80 eV, as indicated in the inset of Fig. 9

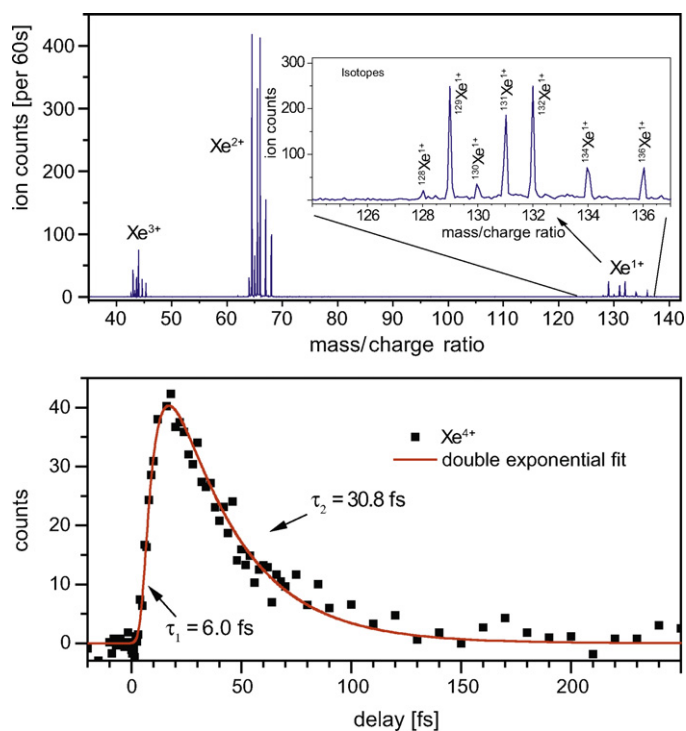


Fig. 8. Upper panel: mass-spectrum recorded in xenon after attosecond XUV excitation with photon energy around 100 eV. Three charge states of xenon are displayed, the relative intensity shows a distinguished correspondence with the interaction cross sections known from synchrotron studies. The inset shows a close up of the generated Xe^+ ions. Seven isotopes can be discriminated; there are two more (mass 124 and 126, respectively) with natural abundances below 0.1%. The resolution of the spectrometer is specified as $\Delta m/m = 10^{-3}$. In the presence of a strong laser pulse, a part of the Xe^{3+} population can be transferred to Xe^{4+} . The temporal evolution of this population reveals the characteristic time structure of two Auger processes.

(upper panel). The exposure time of each of the recorded spectra amounted to 30 s. In order to achieve the reported visibility of characteristic absorption features in the spectrum of the XUV pulse upon its propagation through the gas target, a quasi static gas target, similar to the one used for high-order harmonic generation, had been used instead of a diffusive gas nozzle which is used for attosecond streaking experiments. Due to the inner diameter of the quasi-static gas cell, confinement of the interaction volume between NIR pump and attosecond probe pulses amounts to 1 mm along the beam axis. Fig. 9 (lower panel) displays the extracted absorbance of the XUV pulse based on the two XUV spectra shown in the graph above. Several resonant absorption lines are clearly discernible from non-resonant absorption areas, whereas we can identify the distinct absorption lines as core-to-valence shell transitions triggered by the XUV pulse in Kr^+ and Kr^{2+} . The spectral resolution of ~ 350 meV at 80 eV was limited by the almost fully opened entrance slit of the spectrometer.

Extending this experiment to other atomic or molecular [1,4,5] systems by customizing, within certain limitations, the central energy of the attosecond pulse to the spectral needs of the system of interest, the characteristic information of quantum level populations and, if applicable, subsequent coherent dynamics within the irradiated system can be extracted by tracing the characteristic absorption features on an attosecond time scale. Since the determination of quantum level populations after the strong-field interaction are also accessible by conventional time integrated spectroscopy or transient absorption studies utilizing trains of attosecond pulses [55], this attosecond transient absorption spectroscopic approach is able to address sub-cycle ionization dynamics

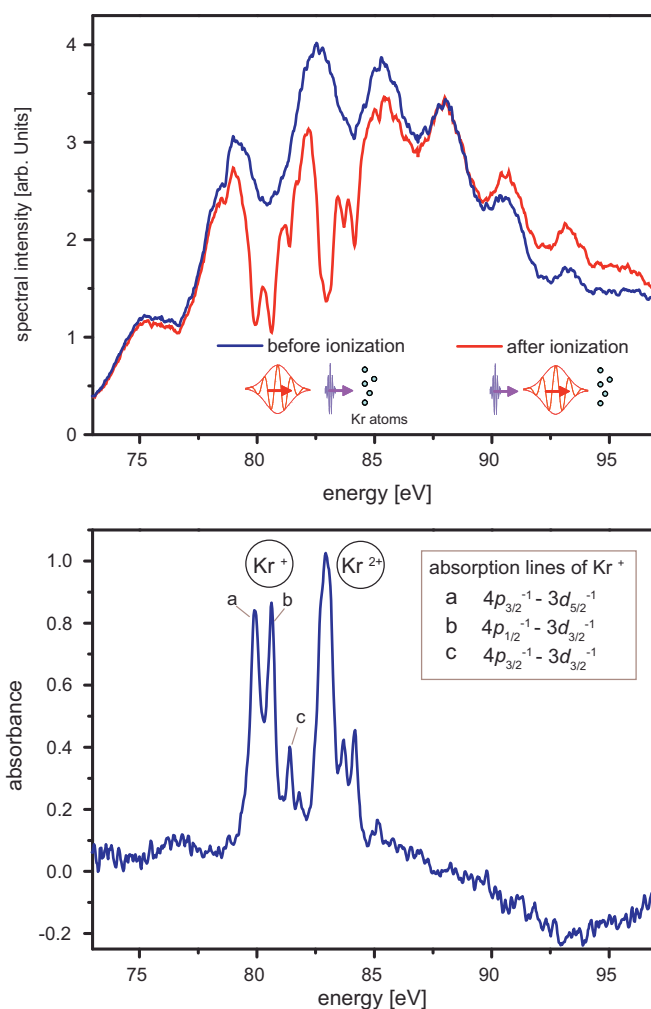


Fig. 9. Exemplary XUV attosecond transient absorption spectra of an attosecond probe pulse centered at ~ 80 eV and propagated through a krypton (Kr) gas target (upper panel). Blue (orange) curve shows the recorded XUV spectrum before (after) ionization of the gas target by a sub-4 fs NIR pump pulse at 5.5×10^{14} W/cm². System-specific absorption signatures in the XUV spectrum arise from the absorption properties of the probed ensemble of neutral and strong-field generated charged states of Kr as displayed in the lower panel. Besides absorption lines of Kr^+ and Kr^{2+} also a region of negative absorbance between 89 eV and 98 eV arises from the NIR-reduced number density of neutral Kr absorbers. Identified absorption lines of Kr^+ are further specified in terms of transitions in the inset of the lower panel where the superscript -1 denotes one missing electron in the corresponding term. The total angular momentum of the ion is given by the subscript. As shown above, the broad XUV spectrum of the attosecond probe pulse allows for simultaneous tracking of absorption features of different charge states as a function of NIR pump–XUV probe delay. (For interpretation of the references to color in this figure legend, the reader is referred to the web version of this article.)

as well as to time-resolve coherent superpositions in the valence shell of atoms. Thus, it can completely and quantitatively retrieve strong-field created electronic coherences as reported in [56].

14. Conclusion and outlook

We have presented a complete experimental setup for attosecond metrology and spectroscopy based on a laser system that provides intense quasi-monocycle laser pulses and a beamline geared for experiments that require attosecond resolution. The beamline combines the merits of attosecond sources with conventional spectroscopic approaches that can enable complete insight into electronic processes in atoms, molecules and solids.

Acknowledgements

This work is supported by the Max Planck Society and the Deutsche Forschungsgemeinschaft Cluster of Excellence: Munich Centre for Advanced Photonics (www.munich-photonics.de) and the KSU-MPQ collaboration.

References

- [1] B.H. Muskatel, F. Remacle, R.D. Levine, *Phys. Scr.* 80 (2009) 048101.
- [2] M. Drescher, M. Hentschel, R. Kienberger, M. Uiberacker, V. Yakovlev, A. Scrinzi, Th. Westerwalbesloh, U. Kleineberg, U. Heinzmann, F. Krausz, *Nature* 419 (2002) 803.
- [3] A.L. Cavalieri, et al., *Nature* 449 (2007) 1029.
- [4] P. Eckle, et al., *Science* 322 (2008) 1525.
- [5] T. Remetter, P. Johnsson, J. Mauritsson, K. Varju, Y. Ni, F. Lepine, E. Gustafsson, M. Kling, J. Khan, R. Lopez-Martens, K.J. Schafer, M.J.J. Vrakking, A. L'Huillier, *Nat. Phys.* 2 (2006) 323.
- [6] M. Hentschel, R. Kienberger, C. Spielmann, G.A. Reider, N. Milosevic, et al., *Nature* 414 (2001) 509–513.
- [7] R. Kienberger, E. Goulielmakis, M. Uiberacker, A. Baltuška, V.S. Yakovlev, et al., *Nature* 427 (2004) 817–821.
- [8] T. Fuji, J. Rauschenberger, A. Apolonski, V.S. Yakovlev, G. Tempea, et al., *Opt. Lett.* 30 (2005) 332–334.
- [9] J. Rauschenberger, T. Fuji, M. Hentschel, A.-J. Verhoef, T. Udem, et al., *Laser Phys. Lett.* 3 (2006) 37–42.
- [10] T. Fuji, J. Rauschenberger, C. Gohle, A. Apolonski, T. Udem, et al., *New J. Phys.* 7 (2005) 116.
- [11] A.L. Cavalieri, E. Goulielmakis, B. Horvath, W. Helml, M. Schultze, M. Fieß, V. Pervak, L. Veisz, V.S. Yakovlev, M. Uiberacker, A. Apolonski, F. Krausz, R. Kienberger, *New J. Phys.* 9 (2009) 242.
- [12] M. Nisoli, S. De Silvestri, O. Svelto, R. Szipöcs, K. Ferencz, Ch. Spielmann, S. Sartania, F. Krausz, *Opt. Lett.* 22 (1997) 522–524.
- [13] A.B. Fedotov, E.E. Serebryannikov, A.M. Zheltikov, *Phys. Rev. A* 76 (2007) 053811.
- [14] V. Pervak, A.V. Tikhonravov, M.K. Trubetskov, S. Naumov, F. Krausz, et al., *Appl. Phys. B* 87 (2007) 5–12.
- [15] TEM Messtechnik GmbH, <http://www.tem-messtechnik.de/>.
- [16] R. Holzwarth, Th. Udem, T.W. Hänsch, J.C. Knight, W.J. Wadsworth, P.St.J. Russell, *Phys. Rev. Lett.* 85 (2000) 2264.
- [17] D.J. Jones, S.A. Diddams, J.K. Ranka, A. Stentz, R.S. Windeler, J.L. Hall, S.T. Cundiff, *Science* 288 (2000) 635.
- [18] C. Gohle, J. Rauschenberger, T. Fuji, T. Udem, A. Apolonski, et al., *Opt. Lett.* 30 (2005) 2487–2489.
- [19] A. Baltuska, et al., *IEEE J. Sel. Top. Quantum Electron.* 9 (4 (July–August)) (2003) 972–989.
- [20] A.J. Verhoef, Method and device for carrier envelope phase stabilization, Patent No. PCT/EP2006/11561.
- [21] T. Wittmann, B. Horváth, W. Helml, M.G. Schätzel, X. Gu, A. Cavalieri, G.G. Paulus, R. Kienberger, *Nat. Phys.* 5 (2009) 357.
- [22] C. Rullière (Ed.), *Femtosecond Laser Pulses: Principles and Experiments*, second ed., Springer, New York, USA, 2005.
- [23] D. Kane, R. Trebino, *IEEE J. Quantum Electron.* 29 (1993) 571–579.
- [24] U. Graf, M. Fieß, M. Schultze, R. Kienberger, F. Krausz, E. Goulielmakis, *Opt. Expr.* 16 (23) (2008) 18956–18963.
- [25] E. Goulielmakis, et al., *Science* 320 (2008) 1614.
- [26] P. Corkum, *Phys. Rev. Lett.* 71 (1993) 1994–1997.
- [27] T. Brabec, F. Krausz, *Rev. Mod. Phys.* 72 (545) (2000).
- [28] M. Schnürer, Z. Cheng, M. Hentschel, F. Krausz, T. Wilhein, D. Hambach, G. Schmahl, M. Drescher, Y. Lim, U. Heinzmann, *Appl. Phys. B* 70 (2000) S227–S232.
- [29] M. Schnürer, Z. Cheng, M. Hentschel, F. Krausz, T. Wilhein, D. Hambach, G. Schmahl, M. Drescher, Y. Lim, U. Heinzmann, *Appl. Phys. B* 70 (7) (2000) 227.
- [30] M. Lewenstein, P. Balcou, M.Y. Ivanov, A. L'Huillier, P. Corkum, *Phys. Rev. A* 49 (1994) 2117–2132.
- [31] L. Poletto, G. Tondello, P. Villoresi, *Rev. Sci. Instrum.* 72 (2001) 2868.
- [32] H. Geiger, W. Müller, *Naturwissenschaften* 16 (31) (1928) 617.
- [33] The Center for X-Ray Optics at the Lawrence Berkeley National Laboratory, <http://www-cxro.lbl.gov/>.
- [34] A. Wonisch, U. Neuhäusler, N.M. Kabachnik, T. Uphues, M. Uiberacker, V. Yakovlev, F. Krausz, M. Drescher, U. Kleineberg, U. Heinzmann, *Appl. Opt.* 45 (17) (2005) 4147–4156.
- [35] Micos GmbH, <http://www.micos-online.com/>.
- [36] T. Harada, H. Sakuma, K. Takahashi, T. Watanabe, H. Hara, T. Kita, *Appl. Opt.* 37 (1998) 6803–6810.
- [37] N. Nakano, H. Kuroda, T. Kita, T. Harada, *Appl. Opt.* 23 (1984) 2386.
- [38] D. Charalambidis, P. Tzallas, E.P. Benis, E. Skantzakis, G. Maravelias, L.A.A. Nikolopoulos, A.P. Conde, G.D. Tsakiris, *New J. Phys.* 10 (2008) 025018.
- [39] M. Hofstetter, M. Schultze, M. Fieß, et al., *Optics Express* 19 (3) (2011) 1767–1776.
- [40] U. Becker, D.A. Shirley, *VUV and Soft-X-ray Photoionization*, Plenum Press, New York, 1996.
- [41] M. Schultze, E. Goulielmakis, M. Uiberacker, M. Hofstetter, J. Kim, D. Kim, F. Krausz, U. Kleineberg, *New J. Phys.* 9 (243) (2007).
- [42] Time-of-flight (TOF) Spectrometers manufactured by Stefan Kaesdorf, Geräte für Forschung und Industrie, <http://www.kaesdorf.brd.de/>.
- [43] FAST ComTec Communication Technology GmbH, <http://www.fastcomtec.com/>.
- [44] J. Itatani, F. Quéré, G.L. Yudin, M.Yu. Ivanov, F. Krausz, P.B. Corkum, *Phys. Rev. Lett.* 88 (2002) 173903.
- [45] Y. Mairesse, F. Quéré, *Phys. Rev. A* 71 (2005) 0011401(R).
- [46] J. Gagnon, E. Goulielmakis, V.S. Yakovlev, *Appl. Phys. B* 92 (2008) 25–32.
- [47] J. Gagnon, V.S. Yakovlev, *Opt. Expr.* 17 (2009) 17678–17693.
- [48] G. Sansone, E. Benedetti, F. Calegari, C. Vozzi, L. Avaldi, et al., *Science* 314 (2006) 443–446.
- [49] E. Goulielmakis, M. Uiberacker, R. Kienberger, A. Baltuška, V.S. Yakovlev, et al., *Science* 305 (2004) 1267–1269.
- [50] M. Schultze, et al., *Science* 328 (2010) 1658–1662.
- [51] M. Uiberacker, et al., *Nature* 446 (2007) 627–632.
- [52] Th. Uphues, M. Schultze, M.F. Kling, M. Uiberacker, S. Hendel, U. Heinzmann, N.M. Kabachnik, M. Drescher, *New J. Phys.* 10 (2008) 2.
- [53] M. Wagner, H. Schröder, *J. Mass Spectrom.* 128 (1–2) (1993) 31–45.
- [54] M. Schultze, B. Bergues, H. Schröder, F. Krausz, K.L. Kompa, *New J. Phys.* in press.
- [55] Z.-H. Loh, et al., *Phys. Rev. Lett.* 98 (2007) 143601.
- [56] E. Goulielmakis, et al., *Nature* 466 (2010) 739–743.